

Article

Effects of K_2TiF_6 and Electrolyte Temperatures on Energy Consumption and Properties of MAO Coatings on 6063 Aluminum Alloy

Xiaomeng Xie ^{1,2}, Erhui Yang ^{1,3}, Ziying Zhang ¹, Wu Wei ¹, Dong Li ¹, Xiaolian Zhao ¹, Ruixia Yang ^{1,*} 
and Weizhou Li ^{1,2,*}

¹ School of Resources Environment and Materials, Guangxi University, Nanning 530004, China

² School of Materials Science and Engineering, Xiamen University of Technology, Xiamen 361024, China

³ School of Mechanical and Marine Engineering, Beibu Gulf University, Qinzhou 535011, China

* Correspondence: yrx20070018@gxu.edu.cn (R.Y.); wzli@xmut.edu.cn (W.L.)

Abstract: To decrease energy consumption and improve the performance of micro-arc oxidation (MAO) films on 6063 Al alloy, a policy of K_2TiF_6 additive and electrolyte temperature control was adapted. The specific energy consumption relied on the K_2TiF_6 additive and more particularly on the electrolyte temperatures. Scanning electron microscopy demonstrates that electrolytes with 5 g/L K_2TiF_6 can effectively seal the surface pores and increase the thickness of the compact inner layer. Spectral analysis shows that the surface oxide coating consists of $\gamma-Al_2O_3$ phase. Following 336 h of the total immersion process, the impedance modulus of the oxidation film, prepared at 25 °C (Ti5-25), remained $1.08 \times 10^6 \Omega \cdot cm^2$. Moreover, Ti5-25 has the best performance/energy-consumption ratio with a compact inner layer ($2.5 \pm 0.3 \mu m$). This research found that the time of the big arc stage increased with the temperature, resulting in producing more internal defects in the film. In this work, we employ a dual-track strategy of additive and temperature providing an avenue to reduce the energy consumption of MAO on alloys.

Keywords: micro-arc oxidation; dipotassium titanium hexafluoride; electrolyte temperature; energy-consumption; corrosion resistance



Citation: Xie, X.; Yang, E.; Zhang, Z.; Wei, W.; Li, D.; Zhao, X.; Yang, R.; Li, W. Effects of K_2TiF_6 and Electrolyte Temperatures on Energy Consumption and Properties of MAO Coatings on 6063 Aluminum Alloy. *Materials* **2023**, *16*, 1830. <https://doi.org/10.3390/ma16051830>

Academic Editors: Ashish Kumar, Chandrabhan Verma and Costica Bejinariu

Received: 7 January 2023

Revised: 11 February 2023

Accepted: 21 February 2023

Published: 23 February 2023



Copyright: © 2023 by the authors. Licensee MDPI, Basel, Switzerland. This article is an open access article distributed under the terms and conditions of the Creative Commons Attribution (CC BY) license (<https://creativecommons.org/licenses/by/4.0/>).

1. Introduction

As a non-ferrous structural material, aluminum alloy is one of the most widely used in industry, for instance, in electronic communication, textiles, automobile, shipping, aviation and other fields. Nevertheless, weak corrosion and wear resistance of aluminum alloy have always restricted its development. Micro-arc oxidation is a surface processing technique with great promise. The ceramic oxide film formed in situ on aluminum alloy by using environmentally friendly electrolyte [1], improves the properties of aluminum alloy [2–5]. The MAO is carried out under the condition of high current and high voltage, so this technology has the disadvantages of high energy consumption and low energy utilization efficiency, which hinders its further development and application [6]; At the same time, owing to the use of traditional MAO basic electrolytes, there are a lot of pores and cracks in these MAO films [7–9], allowing the corrosion medium to easily penetrate into the substrate, which causes corrosion. Therefore, finding a method that can not only reduce energy consumption, but also improves corrosion resistance has become a requirement in the development of MAO technology.

At present, MAO often balances performance and energy consumption by adjusting power parameters and optimizing the electrolyte formula. Changing the current output mode, the current step-down mode uses about 10% less energy than the constant current mode [10]. Compared with the MAO process, the low-energy MAO process with relatively

low voltage (~100 V) can save about 57.0% of energy [11]. Changing the ratio of the anode current to a cathode current (Rpn), the transition to soft plasma [12], changing the power supply mode [13], decreasing the duty cycle and oxidation time [14] and preparing an anodic oxidation prefabricated film [15,16], all of these can cut down the energy consumption of the MAO treatment. Nevertheless, the gain in the energy utilization rate is not obvious because of the regulating electrical parameters. In contrast, optimizing the electrolyte composition can significantly reduce the energy consumption and improve the film's properties. Cheng et al. [17] found that the energy consumption of the MAO process on Al-Cu-Li alloy in electrolytes containing 5, 32 and 56 g·L⁻¹ NaAlO₂ were 13.1~16.7, 3.3~4.8 and 1.1~1.5 kW·h·m⁻²·μm⁻¹, respectively. Following the investigation, we have not found anyone who has studied the influence of K₂TiF₆ additive on the energy consumption of micro-arc oxidation. Most MAO coatings prepared on aluminum alloys are mainly composed of alumina and other solution-related compounds, such as SiO₂, aluminum phosphate and mullite [14,18]. These compounds do not provide enough corrosion protection for the substrate, which make the substrate corrode easily [3,7]. Rahmati et al. [19] studied the coating formation, pore sealing mechanism and properties of AZ31 magnesium alloy MAO in silicate electrolytes containing K₂TiF₆. Adding K₂TiF₆ increased the average thickness of the MAO film, reduced the porosity and formed a thin fluoride-rich passive layer. During the discharge process, TiO₂ particles entered the discharge channel to form a thick and dense coating. The incorporation of SiO₃²⁻ formed amorphous silica in the MAO film, which also sealed some pores in the coating. Therefore, the coating still had high long-term corrosion resistance. Therefore, the addition of K₂TiF₆ could form a denser and thicker MAO film on aluminum alloy, thus improving the corrosion resistance of aluminum alloy and reducing the energy consumption. At the same time, the film contained titanium dioxide, which gave it greater application prospects for biologically related materials [20], as well as photocatalysis [21] and anticorrosion properties [22].

During the MAO process, the electrolyte temperature also influenced the properties of the MAO film. The MAO electrolyte temperature significantly affected the growth and thickness of the ceramic coating [23]. In low-temperature alkaline aluminate electrolytes, more α-Al₂O₃ was formed in the coating, resulting in a high wear resistance and low porosity [24]. Mohannad et al. [25] researched the micro-morphology of MAO film on 6061 aluminum alloy in an alkali silicate solution at different temperatures. It was indicated that the electrolyte temperature affected the characterization of the coating surface. In the electrolyte with a low temperature, a volcano-like structure made up of accumulated particles was formed on the coating surface. The MAO alumina ceramics prepared in the electrolyte with a high temperature were rough, thin and contained grainy spherical hollow bulgy structures, while the pore density, silicon content and infrared emissivity were all high. Therefore, the electrolyte temperature was markedly affected by the MAO coating.

Sreekanth [26,27] studied the effect of adding K₂TiF₆ to silicate electrolytes on the morphology and corrosion resistance of ZM21 and AZ31 magnesium alloys, but did not pay attention to the electrolyte temperature. Tang [28,29] researched the effect of adding K₂TiF₆ on the morphology and corrosion resistance of MAO coating on 2A70 aluminum alloy and AZ91D magnesium alloy at the electrolyte temperature of 40 °C, but did not consider the impact of the electrolyte temperature. Fernandez [30] recently discussed the influence of K₂TiF₆ on the morphology, wear resistance and corrosion resistance of the MAO coating of a secondary casting Al-Si alloy when the electrolyte temperature was controlled at 7 °C. Unfortunately, the influence of the electrolyte temperature was not investigated in depth.

This paper aims to investigate the morphology, structure, energy consumption and properties of MAO film on 6063 Al alloy produced by adding 5 g/L K₂TiF₆ and controlling the average electrolyte temperature at 15 °C, 25 °C and 35 °C, respectively. At the same time, the synergistic effect of the electrolyte temperature and K₂TiF₆ on the growth process and mechanism of the coating is also discussed. In this study, combining the temperature with the electrolyte formula to obtain a high-performance MAO film with a low energy

consumption on aluminum alloy laid the foundation for the early application of this process in industry.

2. Experiment

2.1. Experimental Materials and Film Fabrication

MAO films were prepared on oblong blocks ($20 \times 15 \times 3 \text{ mm}^3$) of 6063 Al alloy (Si 0.20%, Cu 0.015%, Fe 0.25% and Al balance). All specimens were successively polished with 400#, 1000#, 1500# and 2000# sandpaper, until they acquired a surface roughness of $\approx 0.1 \mu\text{m}$. Then, the specimens were ultrasonically washed in 99.9% anhydrous ethanol followed by warm blowing drying. The dilute alkaline solution was composed of: Na_2SiO_3 (10 g·L), Na_3PO_4 (10 g·L), NaF (2 g·L) and K_2TiF_6 (0 or 5 g·L) as an additive. The average temperatures of the electrolyte were: 15 °C, 25 °C and 35 °C. The composition, temperature, conductivity and pH of the different electrolytes are reported in Table 1. The pretreated aluminum alloy specimens were oxidized for 10 min at a constant current density of $10 \text{ A}\cdot\text{dm}^{-2}$, a 30% duty cycle and a frequency of 400 Hz. Then, the MAO samples were ultrasonically washed in de-ionized water followed by warm blowing drying.

Table 1. Identified codes of the MAO-treated samples and their corresponding electrolyte composition, temperature, conductivity and pH.

Sample/ Coating Code	Electrolyte Composition	Cooling Temperature	Conductivity (κ , mS \pm 0.1)	pH
Ti0-15	10 g/L Na_2SiO_3 , 10 g/L Na_3PO_4 , 2 g/L NaF	15 °C	17.92	12.17
Ti5-15	10 g/L Na_2SiO_3 , 10 g/L Na_3PO_4 , 2 g/L NaF, 5 g/L K_2TiF_6	15 °C	16.79	8.18
Ti5-25	10 g/L Na_2SiO_3 , 10 g/L Na_3PO_4 , 2 g/L NaF, 5 g/L K_2TiF_6	25 °C	17.49	8.11
Ti5-35	10 g/L Na_2SiO_3 , 10 g/L Na_3PO_4 , 2 g/L NaF, 5 g/L K_2TiF_6	35 °C	17.65	8.03

2.2. Coating Characterizations

During the MAO treatments, the discharge behaviors were recorded using a commercial digital camera (Handycam FDR-AX100), operating at 100 frames per second. The thickness of the MAO films was the presented average of 10 measurements taken at diverse positions and measured with a TT260B coating eddy current meter. Meanwhile, the phase composition of the films was confirmed by employing a MiniFlex600-C X-ray diffractor (XRD) at a speed of $6^\circ/\text{min}$, at 40 kV and 150 mA, in the 2θ range of 20° to 80° . We analyzed the morphologies, cross-sections and element composition on the films with a scanning electron microscope (SEM/EDS, SU-8020/X-Max 80). The coating Ti5-15 surface was analyzed using X-ray photoelectron spectroscopy (XPS, Thermo ESCALAB 250XI), and then the XPS curve was fitted using XPSPEAK4.1 software, Version 4.1 November 2000, Raymond Kwok, Shatin, Hong Kong, China.

2.3. Energy Consumption

Through the power signal acquisition system, the specific data of voltage and current changes with the reaction time were obtained, and then the unit energy consumption was calculated according to Equation (1) [31], taking the average of three parallel samples.

$$\rho = \frac{\int_0^T V_t I_t dt}{SL} \quad (1)$$

where ρ is the energy consumption to generate a unit volume of the micro-arc oxide film layer ($\text{kw}\cdot\text{h}\cdot\text{m}^{-2}\cdot\mu\text{m}^{-1}$), V_t as transient voltage (V), I_t as *Transient* current (A) and T as duration time in the MAO process, S as the specimen superficial area (m^2) and L as film thickness (μm).

2.4. Corrosion Behavior of the Films

In 3.5 wt% NaCl solution, we used an electrochemical workstation (CS350, CorrTest) to measure the potentiodynamic polarization (PDP) with a 10 mV/s scanning rate to investigate the corrosion performance. The tests used a saturated calomel electrode and platinum plate as the reference electrode and counter electrode, and 1 cm² of film that was exposed in the NaCl solution as the working electrode. In addition, we used electrochemical impedance spectroscopy (EIS) to investigate the electrochemical behavior of the MAO films. The disturbance amplitude was 10 mV and the frequency ranged from 10⁵ Hz to 0.01 Hz. Some EIS tests were carried out after 336 h of immersion to research the long-term corrosion properties of the specimens. The Zview software was used to analyze the test data.

3. Results

3.1. Evolution of Voltage and Discharge

According to the voltage response curves and the sparks in the reaction stage, we distinguished four typical discharge stages in the MAO treatment: stage I (anodic oxidation), stage II (spark discharge), stage III (micro-arc) and stage IV (big arc) [32]. During stage I, quantities of gas were generated, a barrier film was formed and the metallic luster gradually vanished from the specimens' surface. In stage II, the voltage rose linearly and rapidly, which was maintained for a short time. A large number of fast-walking small white sparks were discovered and the voltage increase rate declined. Entering stage III, these sparks turned yellow, augmented in size and reduced in quantity. Then, the voltage achieved a steadier level and sustained a slow rise. During stage IV, some large arcs with a longer lifetime were observed in the local regions of the specimens.

Figure 1 indicates the evolution of voltage and the spark discharge features of samples Ti0-15, Ti5-15, Ti5-25 and Ti5-35. The effect of the diverse electrolytes to the voltage response curves is prominent [29]. From Figure 1a, samples Ti5-15, Ti5-25 and Ti5-35 with the addition of 5 g/L K₂TiF₆ were different from sample Ti0-15 without K₂TiF₆. In stage I, the voltage of Ti0-15 increased faster than that of Ti5-15, Ti5-25 and Ti5-35, while the voltage of Ti5-15 increased the slowest. Nevertheless, Ti5-15, Ti5-25 and Ti5-35 demonstrated a higher working voltage than Ti0-15 in stage III. The termination voltages of Ti0-15, Ti5-15, Ti5-25 and Ti5-35 were about 441 V, 475 V, 478 V and 450 V, respectively.

From Figure 1b, sparks appeared on Ti5-15, Ti5-25 and Ti5-35 surface within 90 s (~322 V, ~296 V and ~281 V), while sparks appeared on the Ti0-15 surface at 111 s (~366 V), respectively. These consequences exhibited that a dielectric breakdown had occurred on the specimens with 5 g/L K₂TiF₆, as opposed to without K₂TiF₆. The metal surface property, the component and conductivity of the solution strongly influenced the breakdown voltages [28,33]. The discharge phenomenon of Ti0-15 and Ti5-15 was chiefly composed in spark discharge stage and the micro-arc stage that commenced after 130 s. When the average electrolyte temperature was 25 °C, the big arc stage started after 480 s. The big arc stage initially began after 390 s when the electrolyte temperature was 35 °C. The start time of the big arc stage advanced with the increase of the electrolyte temperature, causing a longer big arc stage reaction time.

3.2. Microstructure of the Films

It can be observed from Figure 2a that the micropores on the Ti0-15 surface are relatively smaller and fewer because of the small dimension of the discharges. As can be observed in Figure 2, films Ti5-15, Ti5-25 and Ti5-35, with the addition of 5 g/L K₂TiF₆ had larger dimension pores than film Ti0-15 without K₂TiF₆, that should be ascribed to the involvement of TiO₂ particles in the electrochemical reaction, which caused the coating thickness and working voltages to increase (Figure 1a). The coating surface of Ti5-15 was compact and uniform and the large pores were full of oxide. From Figure 2c,d, there are obvious porous regions, where big pores were distributed in concentration and appeared on the surface when the electrolyte temperatures rose to 25 °C. These porous areas might be formed by the generation of constant and big dimension arcs in defects in the coating

occurring in stage IV. The operation time of stage IV was lengthened with the higher electrolyte temperatures, which brought about the increase of the coverage area of the porous regions and more rough coating surfaces. In addition, the quantity and size of the sparks in the non-porous regions were reduced, because more electric energy was concentrated in the porous regions.

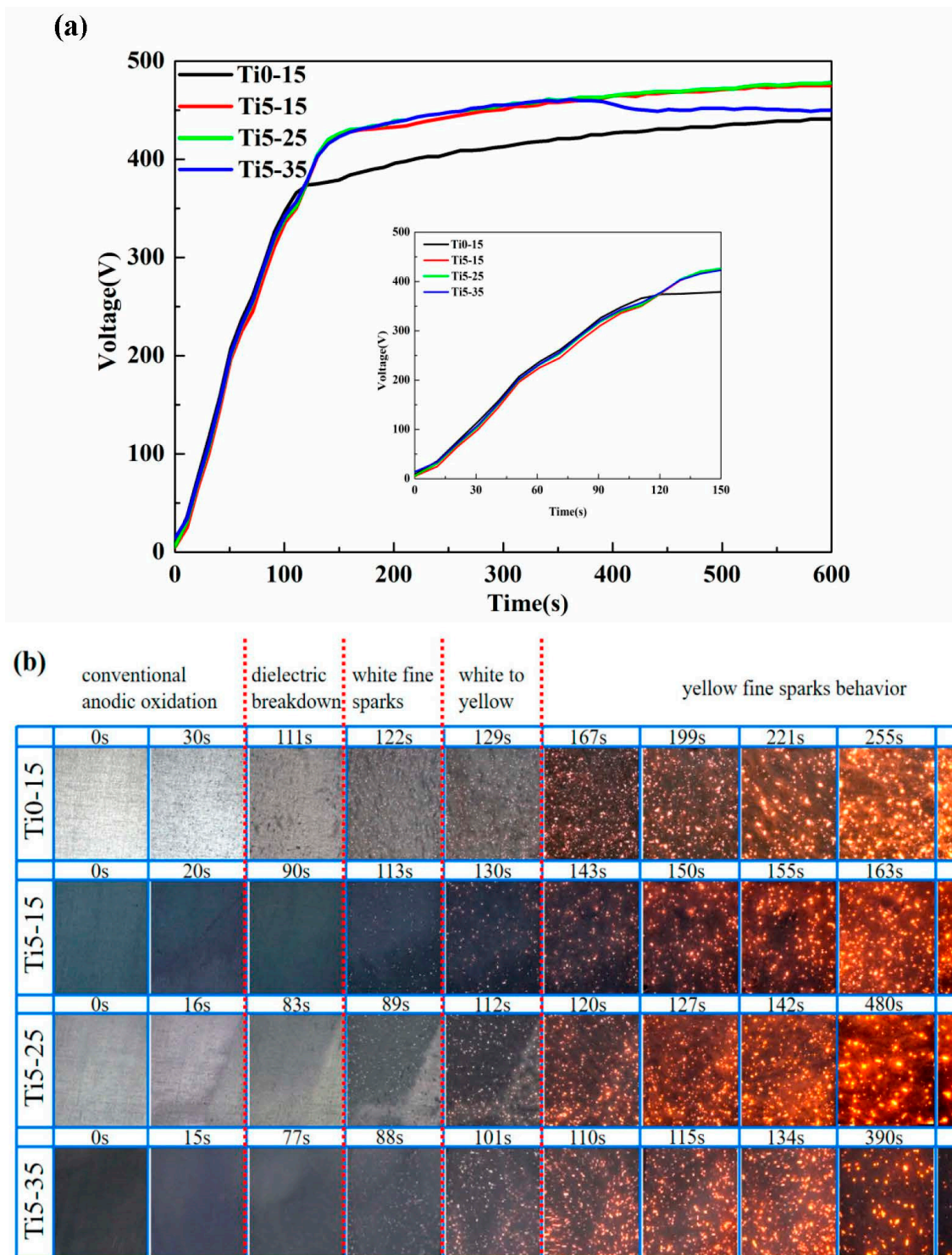


Figure 1. (a) Voltage-time curves and (b) evolution of the micro-discharge of Ti0-15, Ti5-15, Ti5-25 and Ti5-35 micro-arc oxidation for 10 min.

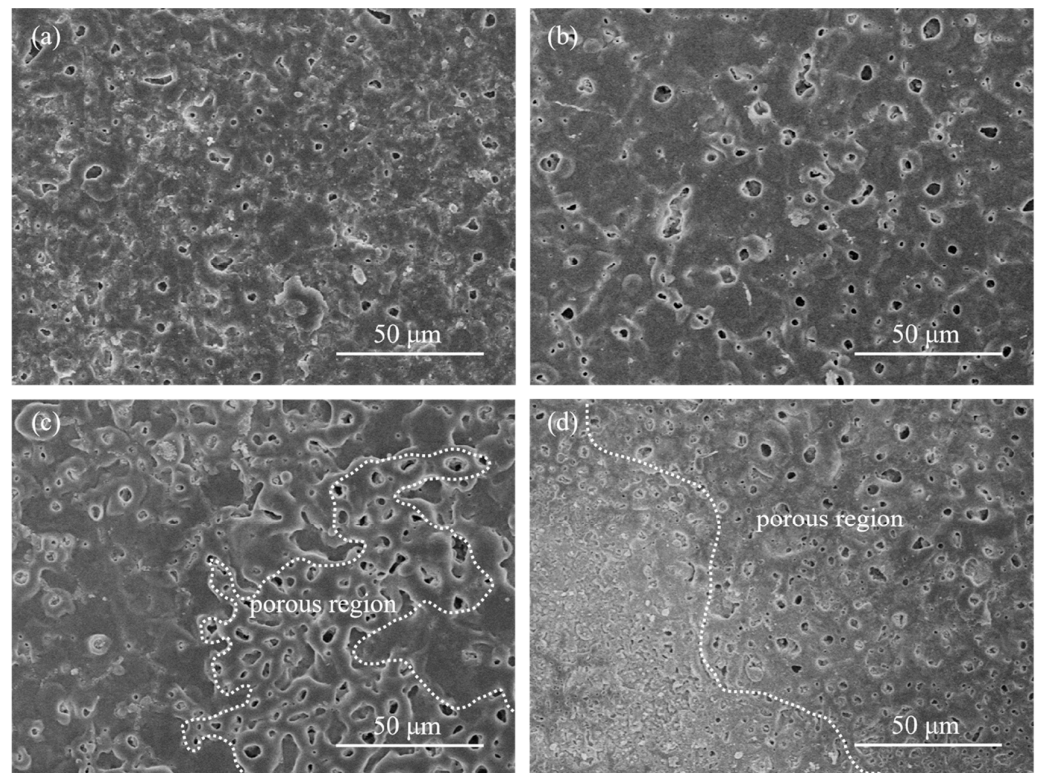


Figure 2. Surface morphology of the MAO film layers of different micro-arc oxidized samples for 10 min: (a) Ti0-15, (b) Ti5-15, (c) Ti5-25 and (d) Ti5-35.

The EDS results of surfaces of films Ti0-15, Ti5-15, Ti5-25 and Ti5-35 are shown in Table 2. Film Ti0-15 without K_2TiF_6 was mostly made up Al and O. The element composition of films Ti5-15, Ti5-25 and Ti5-35 with the addition of 5 g/L K_2TiF_6 all mainly contained Al, O and Ti. With the addition of 5 g/L K_2TiF_6 , the values of the Al mass percent decreased on the surfaces, while that of Ti increased. The values of the Ti mass percent decreased on Ti5-15, Ti5-25 and Ti5-35 surfaces with the elevation of the electrolyte temperature indicating a lower incorporation of Ti in the films [29]. However, the incorporation of the compositions from the solution increased with the elevation of the electrolyte temperature. The lower viscosity with the elevation of the electrolyte temperature led to it becoming easier for the hotter electrolyte to flow to the reaction surface and augmented the direct electrolyte-surface interaction [25]. Moreover, Ti content in Ti5-15, Ti5-25 and Ti5-35 was higher than that in the MAO coatings prepared by Tang [28] and Arunnellaiappan [33] on 2A70 and AA7075 aluminum alloys, by adding potassium fluotitanate. This showed that TiO_2 sol particles could easily enter the coating by this method.

Table 2. EDS results of the surfaces of films Ti0-15, Ti5-15, Ti5-25 and Ti5-35.

Element/wt%	Al	O	Si	P	Na	F	Ti	K
Ti0-15	61.99	28.216	6.129	2.694	0.971	0	-	-
Ti5-15	35.733	29.581	4.523	4.181	1.245	0.516	23.535	0.686
Ti5-25	32.763	28.081	7.042	4.019	4.06	3.824	18.587	1.624
Ti5-35	26.54	27.728	8.904	4.982	8.17	4.086	17.034	2.557

A cooling device was used to keep the cooling water below 15 °C, and 5 g/L K_2TiF_6 was added for the MAO treatment for 120 and 180 s to study the incorporation mechanism of the solution's components. The surface micromorphology of these two coatings were shown in Figure 3. Following treatment for 120 s, it was in the spark discharge stage (the second stage) that the detected O and F content on the surface exceeded that of the other

electrolyte elements (Table 3), that is, other the elements extracted from the electrolytes were very low, indicating generated aluminum fluoride and alumina. In other words, a thin fluorine barrier layer was generated early in the MAO [19]. Following treatment for 180 s and just entering the micro-arc oxidation stage (the third stage), the F content dropped, and the content of other elements increased with the increase of thickness (Table 3), Forming more and larger discharge channel anions. Therefore, a large number of elements in the electrolyte were pulled into the channels of the outer coating after 180 s.

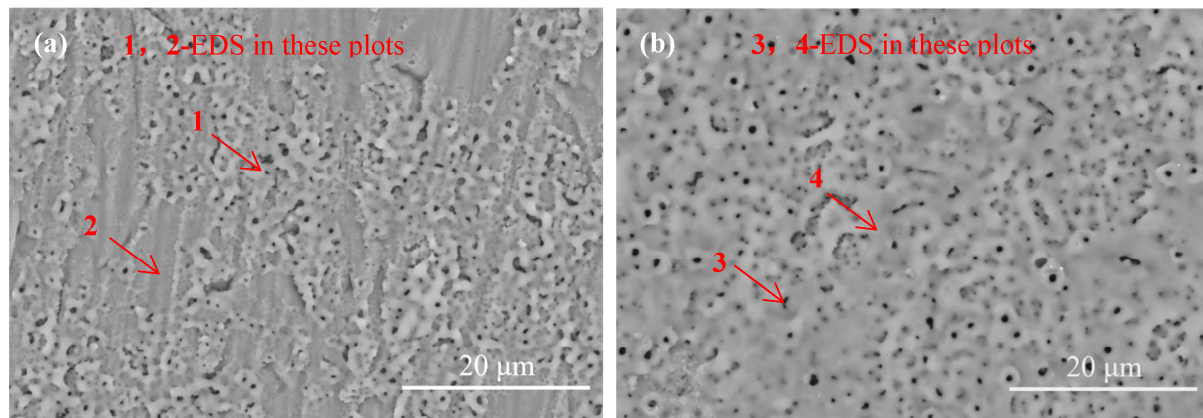


Figure 3. Surface micromorphology of the samples with different treatment times: (a) 120 s and (b) 180 s.

Table 3. EDS results of the coatings for samples with different treatment times.

Element/wt%	Al	O	Si	P	Na	F	Ti	K
90''-surface	58.073	23.413	1.926	2.198	0.148	9.383	4.606	0.242
90''-point1	51.224	31.886	3.147	2.695	0.358	4.965	5.255	0.166
90''-point2	69.767	16.374	0.936	1.014	0.124	10.194	1.536	0.055
130''-surface	39.577	30.77	4.723	3.162	0.622	1.032	19.924	0.19
130''-point3	41.043	26.731	3.694	3.112	0.611	3.896	20.855	0.058
130''-point4	34.810	37.370	6.841	3.075	0.668	0.278	16.814	0.124

Figure 4 displays the cross-sectional morphology and the EDS line scan results of different MAO films. From Figure 4a, there are cavities of different dimensions as a band at the substrate/film interface of Ti0-15. The connected large cavities are formed by the strong spark discharge at the substrate/film interface [5]. There are also plenty of pores of different dimensions and cracks in Ti0-15. The micro discharges and gas bubbles resulted in the formation of micropores. The thermal stress that was formed when the molten oxide solidified rapidly and brought about the generation of microcracks [19,20]. Ti5-15 with a fine continuity, fewer defects and thicker compact inner layer was produced at 15 °C by adding 5 g/L K_2TiF_6 (Figure 4b). The micro discharges of stage III were weak and well-proportioned, which could repair the defects and fill the pores in the films quickly, so the denser films could be acquired by lengthening the stage III operation time. In Figure 4c,d, the quantity and size of the pores of Ti5-25 and Ti5-35 were augmented because of the extension of the stage IV operation time with the increase in electrolyte temperature. The production of big pores and cracks occurred due to the formation of long-lasting, uneven and strong discharge breakdown in the films. The greater thermal stresses were concentrated near the big discharge sparks, so it was hard to repair the defects and fill the pores. This further showed that the longer operation time of stage III is helpful for forming a dense film, while the longer action of stage IV produces more internal defects in the film.

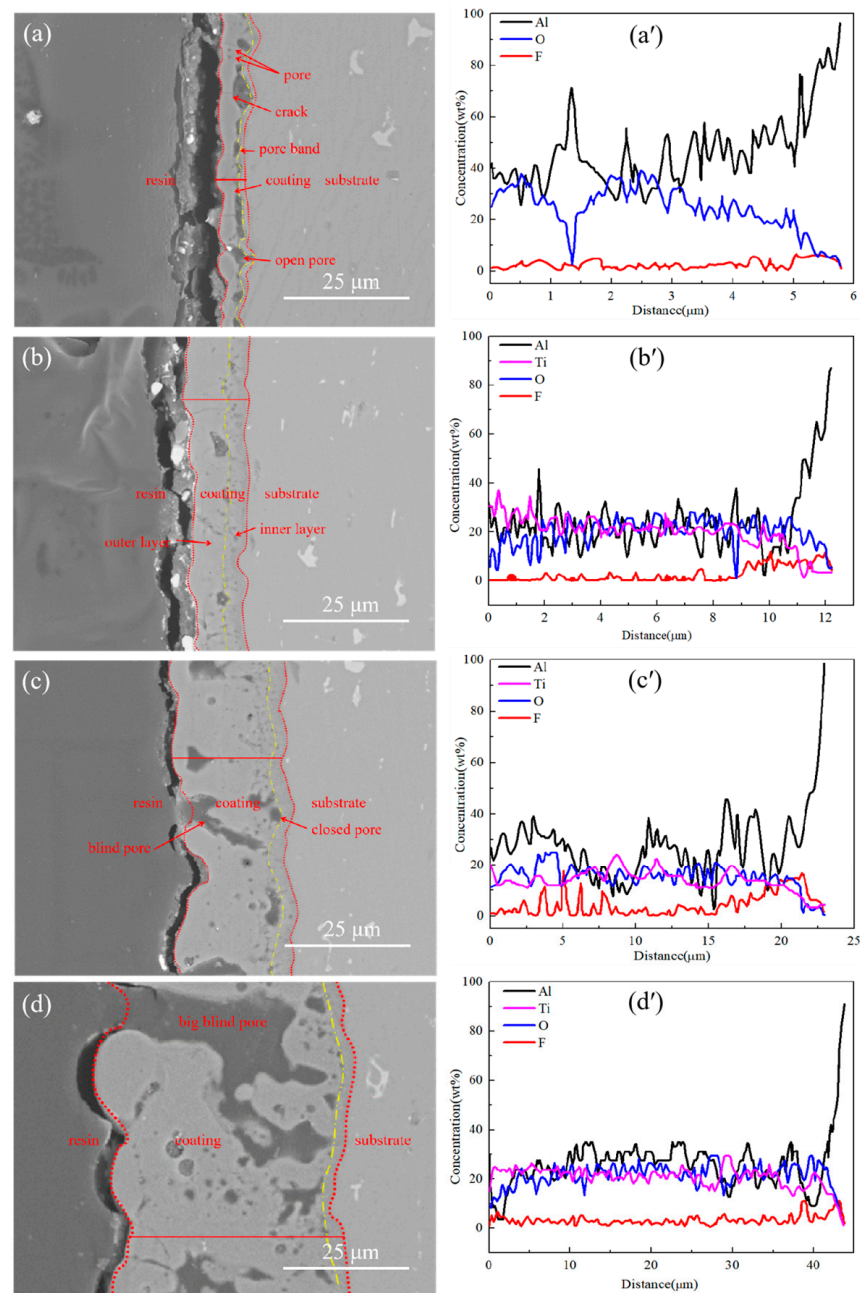


Figure 4. Cross-sectional morphology of MAO films after micro-arc oxidation for 10 min and the elements line distribution examined by EDS: (a,a') Ti0-15, (b,b') Ti5-15, (c,c') Ti5-25 and (d,d') Ti5-35.

The distribution of the elements of the cross-sectional Ti0-15, Ti5-15, Ti5-25 and Ti5-35 obtained by the EDS line scan are shown in Figure 4a'–d'. Al, O and Ti were dispersed nearly evenly across the thickness of the films. The incorporation of the F element obviously increased at the substrate/film interface for all films. The F^- ions were easily congregated at the substrate/film interface and generated the AlF_3 with reaction of Al^{3+} and F^- ions [19]. The mass ratio of aluminum and oxygen in the coating were reduced, while the mass ratio of aluminum in Ti augmented with the addition of 5 g/L K_2TiF_6 . When the electrolyte temperature increased, the mass fraction of Al, Ti and O in Ti5-15, Ti5-25 and Ti5-35 coatings decreased. Consistent with the results of the surface analysis.

The thickness of the films significantly increased with 5 g/L K_2TiF_6 additive and the elevation of the electrolyte temperature due to the increased voltage that accelerated the development of the films. As evidently recognizable from the cross-section micrographs

(Figure 4a–d), the inner and outer layers made up the total MAO film. The compact inner layers of films Ti5-15, Ti5-25 and Ti5-35, with the addition of 5 g/L K_2TiF_6 were thicker than film Ti0-15 without K_2TiF_6 . The coating thicknesses of films Ti0-15, Ti5-15, Ti5-25 and Ti5-35 were $5.8 \pm 0.7 \mu m$, $12.3 \pm 1.0 \mu m$, $21.3 \pm 1.5 \mu m$ and $47.9 \pm 4.1 \mu m$ by TT260B coating eddy current meter, however, the thickness of the compact inner layer of Ti5-15 was the largest, which was $3.9 \pm 0.3 \mu m$ according to the cross-sectional SEM analysis, as shown in Table 4. The thickness increment of the MAO film obtained by combining the temperature and electrolyte formula is higher than that of the coating prepared by adding K_2TiF_6 only [19,29]. This result showed that the growth rate of the coating prepared using this method is greatly improved. Figure 5 revealed the unit energy consumption of Ti0-15, Ti5-15, Ti5-25 and Ti5-35. The energy consumption of Ti5-15, Ti5-25 and Ti5-35 was significantly lower compared to Ti0-15. In Figure 5, the unit energy consumption of Ti5-35 ($1.71 \text{ kw}\cdot\text{h}\cdot\text{m}^{-2}\cdot\mu\text{m}^{-1}$, only 13% of the energy consumption of Ti0-15) was lower. Compared with most of the reported research energy consumption, the energy consumption reduction effect is achieved [10–16]. It demonstrated that both 5 g/L K_2TiF_6 additive and the elevation of electrolyte temperature could increase the coating thickness to reduce the energy consumption.

Table 4. Thickness of the MAO coating inner layer, outer layer and the whole coating of different samples after micro-arc oxidation for 10 min.

Coating Sample Thickness (μm)	Inner Layer		Outer Layer		All Coating	
	Average	Standard Deviation	Average	Standard Deviation	Average	Standard Deviation
Ti0-15	1.2	0.2	4.6	0.5	5.8	0.7
Ti5-15	3.9	0.3	8.5	0.8	12.3	1.0
Ti5-25	2.5	0.3	18.7	1.3	21.3	1.5
Ti5-35	2.0	0.2	44.0	4.0	47.9	4.1

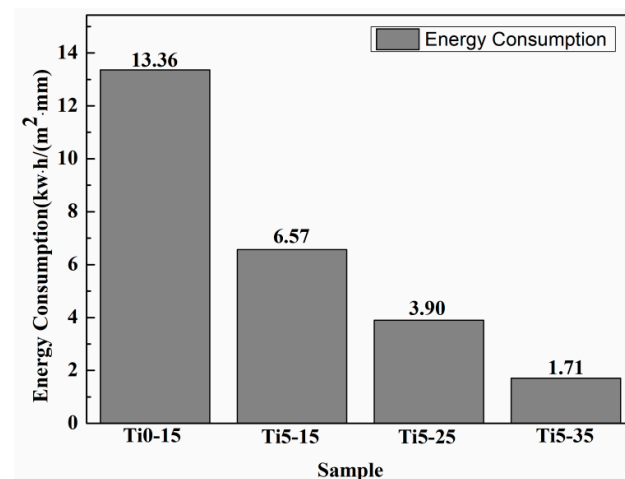


Figure 5. Energy consumption (ρ) for 10 min of micro-arc oxidation for different samples.

3.3. Phase Composition

Figure 6 showed the XRD patterns in which films Ti0-15, Ti5-15, Ti5-25 and Ti5-35 were displayed. It can be observed that the major phases of Ti0-15, Ti5-15, Ti5-25 and Ti5-35 were $\gamma\text{-Al}_2\text{O}_3$, the amorphous phase and Al because of the penetration of XRD through the film to the substrate [25]. With $5 \text{ g}\cdot\text{L}^{-1}$ K_2TiF_6 additive and the increase in the electrolyte temperature, the descent of the XRD peak intensity of Al could be caused by the increase of the coating density and thickness [34]. Nevertheless, the peak intensity of $\gamma\text{-Al}_2\text{O}_3$ decreased and the diffuse scattered peak of the amorphous phase at 2θ within $10\text{--}35^\circ$

increased with $5 \text{ g}\cdot\text{L}^{-1} \text{ K}_2\text{TiF}_6$ additive and the increase in the electrolyte temperature. In other words, Ti0-15 was composed of higher $\gamma\text{-Al}_2\text{O}_3$ but was lower than Ti5-15, Ti5-25 and Ti5-35 in the amorphous phase content. The element Ti was detected in Ti5-15, Ti5-25 and Ti5-35 by EDS, but there were no crystal phase peaks relevant to titanium oxides. This could be attributed to their amorphous structure or low content or the combination of Ti and $\gamma\text{-Al}_2\text{O}_3$ [19,29]. As shown in Figure 7, the XPS spectrum of Ti 2p had a Ti $2p_{3/2}$ peak at 458.7 eV and a Ti $2p_{1/2}$ peak at 464.3 eV, which was consistent with the binding energy of TiO_2 [33]. It was further proved that the MAO coating prepared by adding K_2TiF_6 contains TiO_2 .

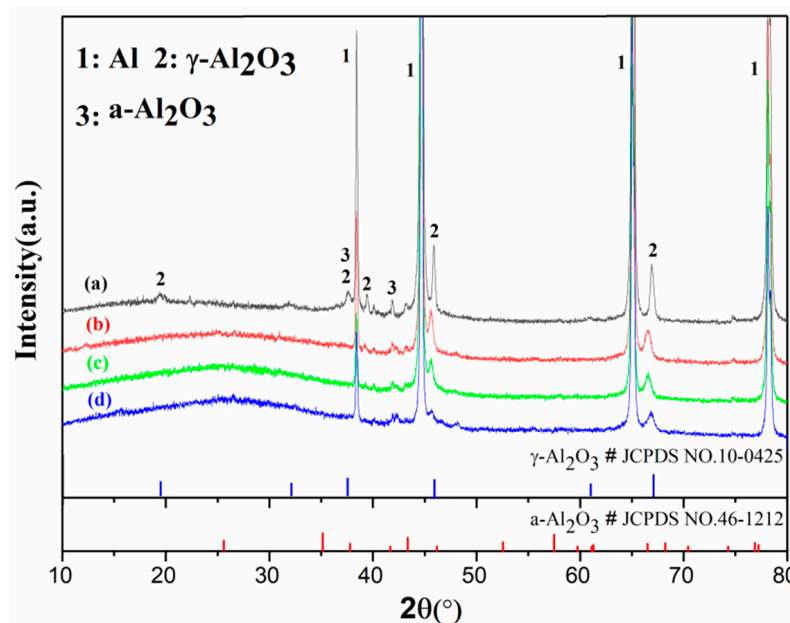


Figure 6. XRD pattern of different MAO films: (a) Ti0-15, (b) Ti5-15, (c) Ti5-25 and (d) Ti5-35.

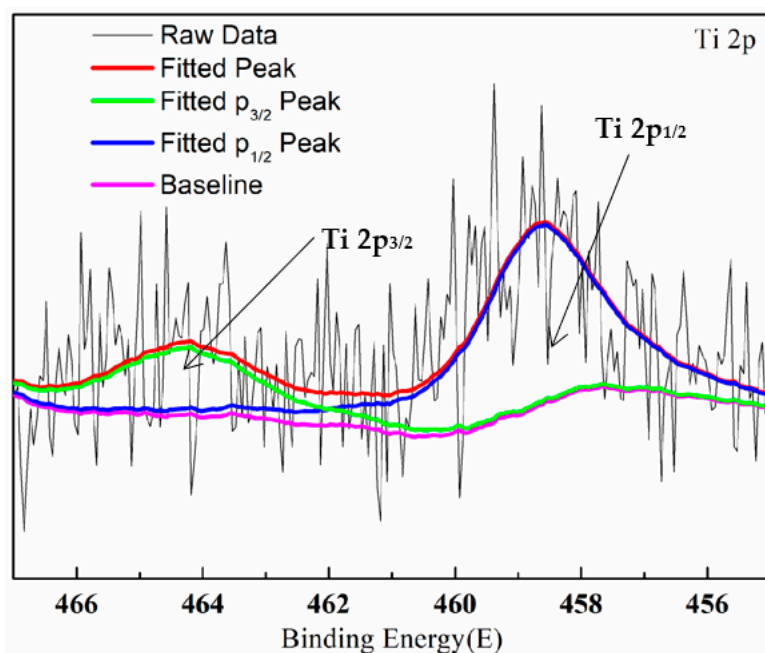


Figure 7. XPS diagram of Ti5-15 MAO film.

3.4. Corrosion Resistance of the Films

The fitting parameter value and PDP of films Ti0-15, Ti5-15, Ti5-25 and Ti5-35 are displayed in Figure 8 and Table 5. From fitting dates and potentiodynamic polarization curves, the self-corrosion current density (i_{corr}) of the MAO coating with added potassium fluotitanate dropped, and the self-corrosion potential (E_{corr}) rose. The self-corrosion current density and corrosion rate of Ti5-15 film were both minimal, which were $7.238 \times 10^{-5} \text{ mA/cm}^2$ and 0.071 mm/a , respectively. Moreover, E_{corr} of Ti5-15 coating achieved -1.183 V , indicating that Ti5-15 film has a good corrosion resistance.

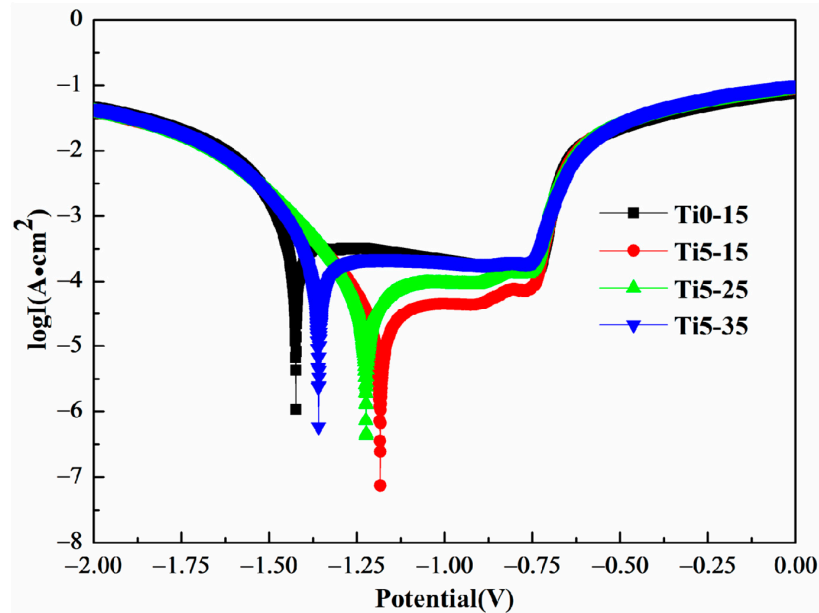


Figure 8. Potentiodynamic polarization curves of coatings Ti0-15, Ti5-15, Ti5-25 and Ti5-35.

Table 5. Fitting data obtained from the polarization curves of coatings Ti0-15, Ti5-15, Ti5-25 and Ti5-35.

Sample	β_a ($\text{mV} \cdot \text{dec}^{-1}$)	β_c ($\text{mV} \cdot \text{dec}^{-1}$)	E_{corr} (V)	i_{corr} ($\text{A} \cdot \text{cm}^{-2}$)	R_{corr} ($\text{mm} \cdot \text{a}^{-1}$)
Ti0-15	3096.2	147.95	-1.424	6.297×10^{-4}	0.617
Ti5-15	11,609	223.62	-1.183	7.238×10^{-5}	0.071
Ti5-25	3260.3	222.67	-1.224	1.354×10^{-4}	0.133
Ti5-35	3930.2	173.9	-1.359	3.545×10^{-4}	0.348

Bode plots of films Ti0-15, Ti5-15, Ti5-25 and Ti5-35 are displayed in Figure 9a–d. Figure 9e shows the variation of impedance values $|Z|_{0.01\text{Hz}}$ at 0.01 Hz with prolonging of the soaking time. All impedance values reduced after a 24 h immersion. It should be noted that Ti0-15 descended quickly, and the impedance value $|Z|_{0.01\text{Hz}}$ dropped two orders of magnitude after a 336 h immersion, demonstrating exacerbation of the film [3]. On the contrary, $|Z|_{0.01\text{Hz}}$ of Ti5-15, Ti5-25 and Ti5-35 slightly increased with the prolonging of the immersion time in the soaking period of 24 h. Maybe this is because of the small dimension and shallow depth of the pores on the surface of Ti5-15, Ti5-25 and Ti5-35, which could be occluded directly by the corrosion products [35]. For this reason, the penetration of corrosion solution into the films was hindered. Following 336 h of the total immersion process, the impedance values $|Z|_{0.01\text{Hz}}$ of Ti5-15 and Ti5-25 remained above $10^6 \Omega \cdot \text{cm}^2$, demonstrating that Ti5-15 and Ti5-25 displayed good corrosion protection. In addition, the low-frequency impedance values of Ti5-15, Ti5-25 and Ti5-35 decreased more slowly than those of the micro-arc oxidation coatings prepared by Rahmati [19] and Fernandez [30] on AZ31 Mg alloy and secondary cast Al-Si alloy. It can be considered that the long-term corrosion resistance of Ti5-15, Ti5-25 and Ti5-35 coatings is better.

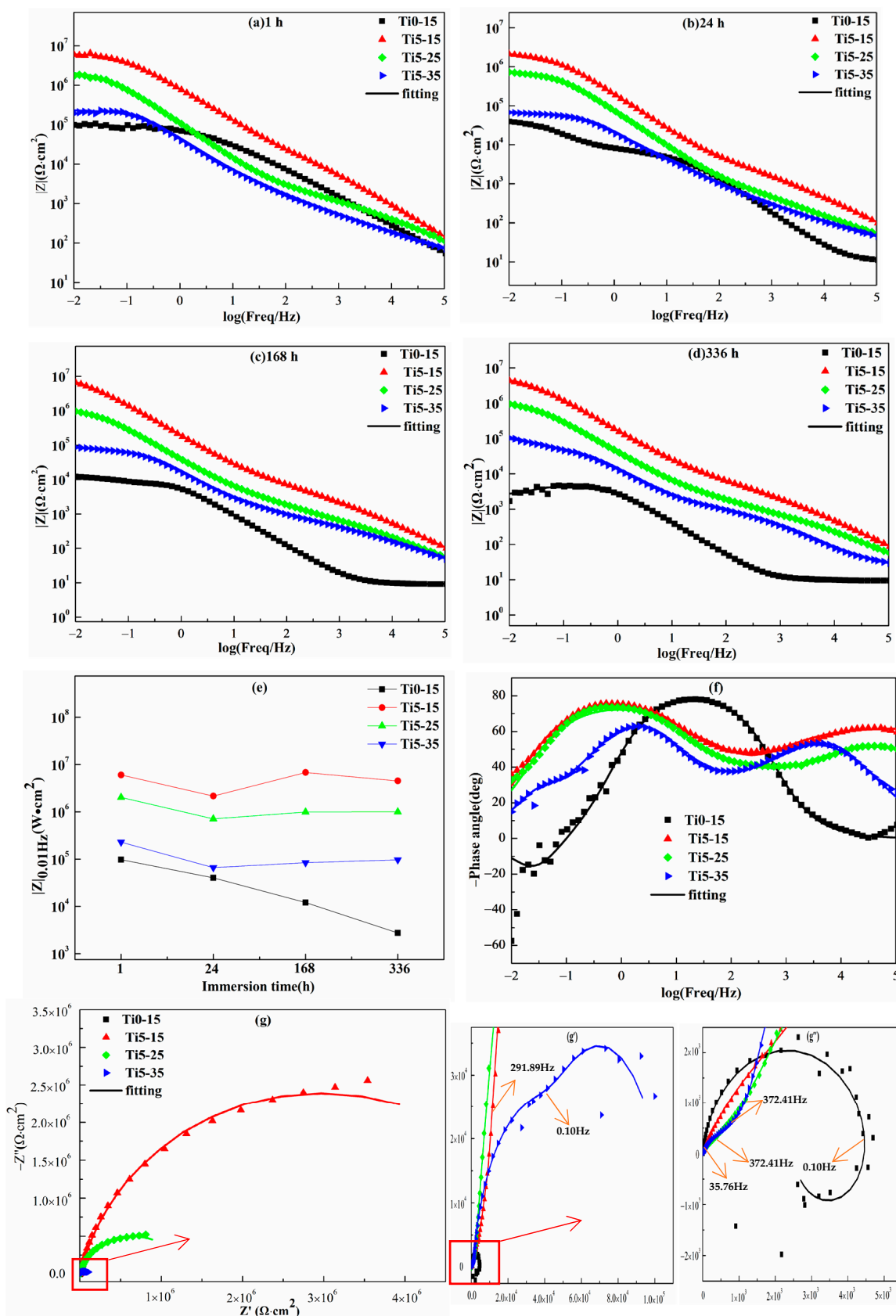


Figure 9. Bode impedance (e) of different MAO coatings treated in 3.5% sodium chloride corrosive medium after (a) 1 h, (b) 24 h, (c) 168 h and (d) 336 h. (e) $|Z|_{0.01\text{ Hz}}$ values of Ti0-15, Ti5-15, Ti5-25 and Ti5-35 after soaking. (f) Phase diagram, (g-g'') Nyquist diagram of Ti0-15, Ti5-15, Ti5-25 and Ti5-35 after soaking for 336 h in 3.5% NaCl solution.

The Nyquist diagram (Figure 9g–g'') and phase (Figure 9f) diagrams of films Ti0-15, Ti5-15, Ti5-25 and Ti5-35 after a 336 h immersion were fitted using three kinds of electrical equivalent circuits (Figure 10) by Zview software. In addition, Table 6 reports the data of the corresponding fitting electrochemical parameters. R_s is the uncompensated solution resistance, R_o , R_i and R_{ct} are the resistance of the outer layer, inner layer and charge transfer, respectively. CPE_o , CPE_i and CPE_{ct} are the capacitance of the outer layer, inner layer and charge transfer, respectively. Y_o , Y_i and Y_{ct} are the admittance constant n_o , n_i and n_{ct} ($0 < n < 1$) are the index of CPE_o , CPE_i and CPE_{ct} . Furthermore, inductor L and R_L were used to indicate the pitting corrosion in the films.

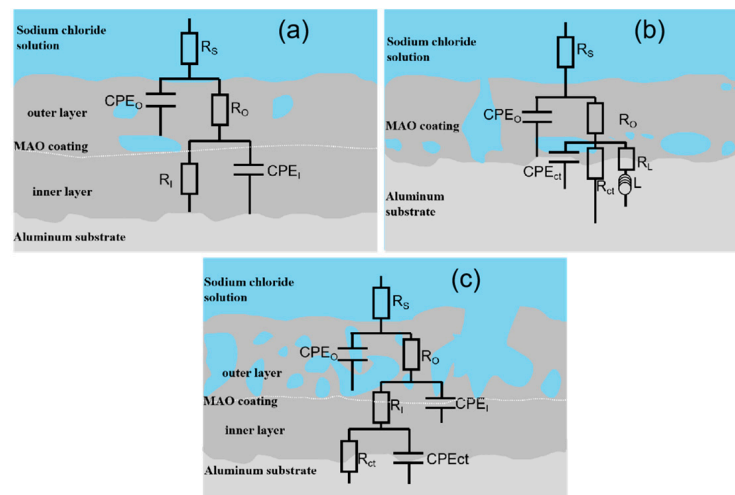


Figure 10. Equivalent circuits used to fit the EIS plots of (a) Ti5-15 and Ti5-25, (b) Ti0-15 and (c) Ti5-35.

Table 6. Electrochemical parameters of EIS of Ti0-15, Ti5-15, Ti5-25 and Ti5-35 soaked in 3.5% sodium chloride solution for 336 h.

Sample	R_s ($\Omega \cdot \text{cm}^2$)	R_o ($\Omega \cdot \text{cm}^2$)	R_i ($\Omega \cdot \text{cm}^2$)	R_{CT} ($\Omega \cdot \text{cm}^2$)	CPE_o		CPE_i		CPE_{ct}		L ($\text{H} \cdot \text{cm}^{-2}$)	Chi Square
					Y_o ($\Omega^{-1} \cdot \text{s}^{n_o} \cdot \text{cm}^{-2}$)	n_o	Y_i ($\Omega^{-1} \cdot \text{s}^{n_i} \cdot \text{cm}^{-2}$)	n_i	Y_{ct} ($\Omega^{-1} \cdot \text{s}^{n_{ct}} \cdot \text{cm}^{-2}$)	n_{ct}		
Ti0-15	10	120	-	226	1.61×10^{-5}	0.92	-	-	3.71×10^{-5}	0.91	950	9.74×10^{-4}
Ti5-15	28	1.01×10^6	5.94×10^6	-	9.49×10^{-7}	0.75	1.22×10^{-6}	0.86	-	-	-	1.01×10^{-3}
Ti5-25	47	1.3×10^5	9.52×10^5	-	6.26×10^{-6}	0.74	4.37×10^{-6}	0.87	-	-	-	1.51×10^{-3}
Ti5-35	16	319	2196	7714	6.2×10^{-6}	0.75	1.14×10^{-5}	0.80	1.23×10^{-6}	0.96	-	1.25×10^{-3}

Following 336 h of immersion, the inductive loop displayed at the low-frequency region for Ti0-15 (Figure 10c). This showed that the beginning of the corrosion of aggressive solution at the substrate and the MAO film should not protect the Al alloy substrate any more. The Nyquist diagram (Figure 9g''), phase diagram (Figure 9f) and equivalent circuit (Figure 10b) diagram of Ti5-35 indicated three-time constants. Thus, it could be deduced that the penetration of the aggressive solution into the film/substrate interface through the micro-pores, indicated the onset of the interface corrosion reaction. Two-time constants were indicated by the electrical equivalent circuit plots of Ti5-15 and Ti5-25 in Figure 10a. This verified the bi-layer structure of the MAO films and the better anti-corrosion property of Ti5-15 and Ti5-25 [7,19]. It can be seen in Table 4, that the resistance values R_o at high frequencies of Ti5-15, Ti5-25 and Ti5-35 were 1.01×10^6 , 1.3×10^5 and $319 \Omega \cdot \text{cm}^2$, respectively, illustrating the resistance value of the outer porous layer was dependent on the composition and microstructure. However, the resistance value R_i at low frequencies of Ti5-15 and Ti5-25 remained high, which were 5.94×10^6 and $9.52 \times 10^5 \Omega \cdot \text{cm}^2$, respectively, which was far higher than R_o . It could be implied that the more compact inner layers were the decisive factor of the anti-corrosion performance of the whole film.

As shown in Figure 11a, after soaking in 3.5% sodium chloride solution for 336 h, Ti0-15 surface had a number of defects and corrosion spots, indicating the dissolution and breakdown of the film initiated in a corrosion pit during the immersion. It was not possible to observe any corrosive defects on the coating surfaces because of the color of the Ti5-15, Ti5-25 and Ti5-35 surfaces were black (Figure 11b,d). The surface micro-graphs of Ti0-15, Ti5-15, Ti5-25 and Ti5-35 were gained by SEM (Figure 11e–i), so that we could observe the corrosion phenomenon clearly. Following immersion for 336 h, Ti0-15 was seriously corroded (Figure 11e). From Figure 11f–i, a black defect was observed on the Ti5-35 surface, while Ti5-15 and Ti5-25 surfaces had almost no obvious abnormalities. This demonstrated the better anti-corrosion property of Ti5-15 and Ti5-25. A lot of white corrosion products were visible on Ti5-15 and Ti5-25, while a few were observed on the Ti5-35 surface, which was consistent with the impedance values of the analysis results.

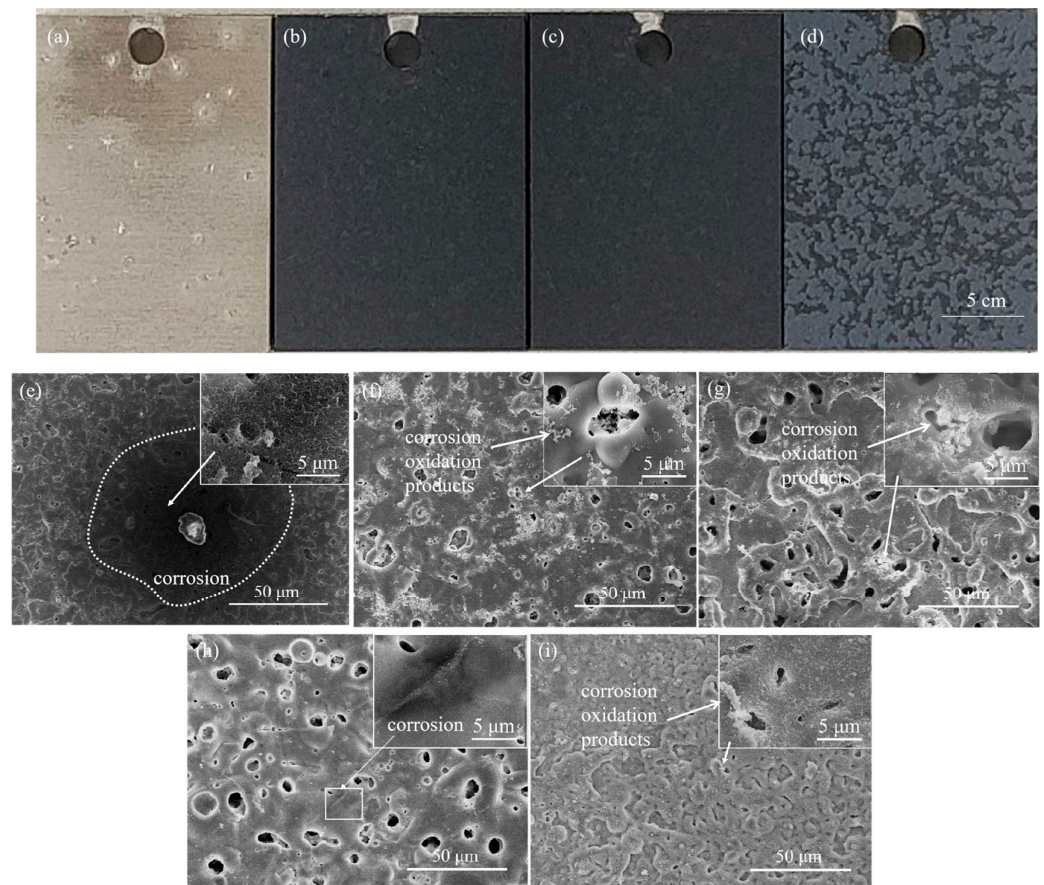


Figure 11. Digital photographs and SEM images of different samples after soaking in 3.5% sodium chloride solution for 336 h: (a,e) Ti0-15, (b,f) Ti5-15, (c,g) Ti5-25 and (d,h,i) Ti5-35.

3.5. Influence of the Electrolyte Temperature on the Coating Growth

Hussein et al. [36] indicated that the MAO discharges could be divided into three types, and Cheng et al. [5] demonstrated that should be four. Discharge type B happens on the alloy/film interface and is strong, discharge type A happens on the film/solution interface, discharge type C happens in the film's surface defects and discharge type D happens in the inner closed pores of the film, respectively, the latter three discharge types belong to the weak discharge. According to the above study and discussions, the MAO film growth mechanism is shown in Figure 12. During stage I (Figure 12a–d), an anodic oxide film was formed by the reaction of Al^{3+} from the alloy and O^{2-} from the solution on the surface and gas was produced [31,37]. F^- migrated from the solution/film interface to the film/alloy interface faster than O^{2-} and hydroxide ions [38], and they generated a

compact barrier layer on the film/alloy interface [19]. Following the addition of $5 \text{ g}\cdot\text{L}^{-1}$ K_2TiF_6 to the solution, the concentration of F increased. Moreover, the migration rate of the anion augmented with the increase of the electrolyte temperature. So that, the anodic oxide film was formed preferentially by adding $5 \text{ g}\cdot\text{L}^{-1}$ K_2TiF_6 and the increase of the electrolyte temperature. This could be proved by the fact that the metallic luster of the Ti-35 surface gradually disappeared after 15 s at the earliest (Figure 1b). Then, the breakdown first occurred on the surface of Ti-35 with a thicker anodic oxidation film (Figure 12h).

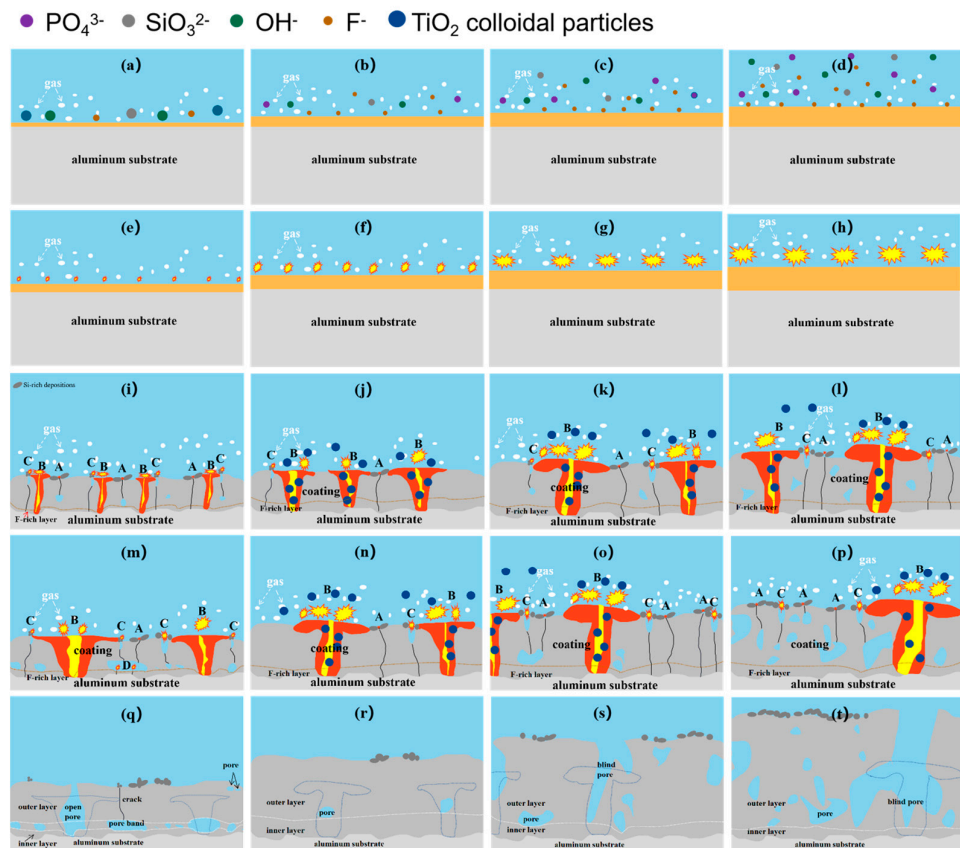


Figure 12. Growth mechanism model of the MAO coatings for different samples: (a,e,i,m,q) Ti0-15, (b,f,j,n,r) Ti5-15, (c,g,k,o,s) Ti5-25 and (d,h,l,p,t) Ti-35.

As shown in Figure 12i–l, the micro-arc stage (stage 3) was the main growth period of the MAO film layer. Within 6 min, the amount and dimension of the discharge channels augmented, type B discharge played a major role, and there were a few types A and C discharges. Once the coating thickened, the number of discharge decreased, but it was more intensive, resulting in large pores on the surface [32]. The coating growth rate increased with the $5 \text{ g}\cdot\text{L}^{-1}$ K_2TiF_6 additive and an increase of electrolyte temperature. Titania colloidal particles were formed by hexafluorotitanate hydrolysis [28]. When the discharge started, these TiO_2 colloidal particles could be drawn into the discharge channels and absorbed and accumulated [29]. The participation of TiO_2 colloidal particles in the reaction increased the coating growth rate [33].

Discharge phenomena of Ti0-15 and Ti5-15 were chiefly composed of the spark discharge and the micro-arc. However, the formation of cavities in Ti0-15 without K_2TiF_6 provided a condition for discharge type D, leading to holes and an increase in cavities (Figure 12m,q). At the temperature of 15°C , the discharge sparks were distributed evenly on Ti5-15 surface (Figure 12n). The liberated heat of Ti5-15 was dissipated uniformly from the coating to the solution. It illustrated that the lower temperature of the electrolyte helped to form a dense and thick film (Figure 12r). The discharge of Ti5-25 entered into the big arc stage at 480 s when the electrolyte temperature rose to 25°C . Therefore, the time of Ti5-25

entering the large arc discharge was short, leading to less aggregation or merging of the arc discharge, which decreased the defects in the film (Figure 12o,s). The starting time of the big arc stage of Ti5-35 was earlier at about 390 s, when the electrolyte temperature rose to 35 °C. Congregation and merging of the arc discharge was obvious by prolonging the big arc stage (Figure 12p). The big discharge sparks were more intensely unevenly distributed, resulting in the concentration of the liberated heat around Ti5-35. For this reason, the electrolyte near Ti5-35 was heated. At this higher temperature, the TiO₂ colloidal particles in the electrolyte tended to aggregate and became unstable [39]. Thus, the compactness of the film was reduced and produced more internal defects (Figure 12t). It could illustrate that the start time of stage IV was earlier with the increase of the electrolyte temperature, resulting in the longer reaction time of stage IV.

4. Conclusions

The titanium dioxide colloidal particles could be driven into the discharge channels by an electric field in a silicate-phosphate mixed based solution containing 5 g/L K₂TiF₆. Thus the addition of 5 g/L K₂TiF₆ can seal some large holes in the film and thicken the film. The occurring time of the big arc stage advanced with the increase of the electrolyte temperature, causing a longer reaction time of the big arc stage, resulting in more rough coating surfaces and more internal defects. The thickness of the entire coating of Ti5-35 was larger than $47.9 \pm 4.1 \mu\text{m}$. Therefore, the unit energy consumption of Ti5-35 was lower than $1.71 \text{ kw}\cdot\text{h}/(\text{m}^2\cdot\mu\text{m})$, which was only 13% of the unit energy consumption of Ti0-15. Both $5 \text{ g}\cdot\text{L}^{-1}$ K₂TiF₆ additive and the elevation of the electrolyte temperature could increase the coating thickness and improve the energy utilization.

The resistance value R_f at low frequencies of Ti-15, Ti-25 and Ti-35 were all higher than the resistance value R_o at high frequencies, indicating that the more compact inner layers were the decisive factor in the anti-corrosion performance of the whole film. Following soaking for 336 h in 3.5% sodium chloride corrosive medium, a black corrosion defect was observed on the Ti5-35 surface, while Ti5-15 and Ti5-25 surfaces had almost no obvious abnormalities. Thus Ti5-25 prepared at 25 °C with the addition of 5 g/L K₂TiF₆ has the best performance/energy-consumption ratio.

The lower electrolyte temperature contributed to prolonging the micro-arc oxidation stage reaction, forming a coating with a fine continuity, fewer defects and a thicker compact inner layer. The operation time of stage IV was lengthened with the higher electrolyte temperatures, which led to more obvious phenomenon of aggregation or merging of the arc discharge and the increase of the coverage area of the porous regions and more rough coating surfaces.

Author Contributions: Methodology, X.X.; Software, X.Z. and Z.Z.; Validation, E.Y., R.Y. and D.L.; Formal analysis, X.X.; Investigation, W.W. and Z.Z.; Resources, W.L.; Data curation, X.X. and D.L.; Writing—original draft, X.X.; Writing—review & editing, R.Y. and W.L.; Visualization, Z.Z.; Supervision, D.L.; Funding acquisition, W.L. All authors have read and agreed to the published version of the manuscript.

Funding: This research was funded by The “Minjiang Scholarship” program of Fujian Province, High-Level Talents Support of Xiamen University of Technology [YKJ22056R, YKJ22059R] and Major Science and Technology Projects in Guangxi [AA18118030].

Data Availability Statement: The data presented in this study are available on request from the corresponding author. The data are not publicly available due to privacy.

Conflicts of Interest: The authors declare no conflict of interest.

References

1. Yerokhin, A.; Shatrov, A.; Samsonov, V.; Shashkov, P.; Pilkington, A.; Leyland, A.; Matthews, A. Oxide ceramic coatings on aluminium alloys produced by a pulsed bipolar plasma electrolytic oxidation process. *Surf. Coat. Technol.* **2005**, *199*, 150–157. [[CrossRef](#)]
2. Peng, Z.; Xu, H.; Liu, S.; Qi, Y.; Liang, J. Wear and Corrosion Resistance of Plasma Electrolytic Oxidation Coatings on 6061 Al Alloy in Electrolytes with Aluminate and Phosphate. *Materials* **2021**, *14*, 4037. [[CrossRef](#)] [[PubMed](#)]

3. Mo, Q.; Qin, G.; Ling, K.; Lv, X.; Wang, N.; Li, W. Layer-by-layer self-assembled polyurea layers onto MAO surface for enhancing corrosion protection to aluminum alloy 6063. *Surf. Coat. Technol.* **2021**, *405*, 126653. [[CrossRef](#)]
4. Lv, X.; Zou, G.; Ling, K.; Yang, W.; Mo, Q.; Li, W. Tribological properties of MAO/MoS₂ self-lubricating composite coating by microarc oxidation and hydrothermal reaction. *Surf. Coat. Technol.* **2021**, *406*, 126630. [[CrossRef](#)]
5. Cheng, Y.-L.; Xue, Z.-G.; Wang, Q.; Wu, X.-Q.; Matykina, E.; Skeldon, P.; Thompson, G. New findings on properties of plasma electrolytic oxidation coatings from study of an Al–Cu–Li alloy. *Electrochim. Acta* **2013**, *107*, 358–378. [[CrossRef](#)]
6. Troughton, S.; Nominé, A.; Henrion, G.; Clyne, T. Synchronised electrical monitoring and high speed video of bubble growth associated with individual discharges during plasma electrolytic oxidation. *Appl. Surf. Sci.* **2015**, *359*, 405–411. [[CrossRef](#)]
7. Qin, G.; Zhang, Y.; Yang, E.; Peng, Z.; Wei, W.; Xie, X.; Li, W. Effect of post-sealing treatment with different concentrations of NaH₂PO₄ on corrosion resistance of MAO coating on 6063 aluminum alloy. *Surf. Coat. Technol.* **2022**, *443*, 128604. [[CrossRef](#)]
8. Sopchenski, L.; Robert, J.; Touzin, M.; Tricoteaux, A.; Olivier, M.-G. Improvement of wear and corrosion protection of PEO on AA2024 via sol-gel sealing. *Surf. Coat. Technol.* **2021**, *417*, 127195. [[CrossRef](#)]
9. Zeng, D.; Liu, Z.; Bai, S.; Wang, J. Influence of Sealing Treatment on the Corrosion Resistance of PEO Coated Al-Zn-Mg-Cu Alloy in Various Environments. *Coatings* **2019**, *9*, 867. [[CrossRef](#)]
10. Yuan, J.; Liu, C.; Xu, T.; Jiang, B.; Li, H.; Yang, B. Effects of current output modes on the growth kinetics and corrosion resistance of micro-arc oxidation coatings on magnesium alloy. *Mater. Res. Express* **2021**, *8*, 066407. [[CrossRef](#)]
11. Tian, H.; Zhang, Y.; Hao, X.; Zhang, H.; Wu, W.; Han, G.; Dou, Z.; Wei, Y.; Zhang, Y.; Chen, F. Preparation and characterization of the low-energy plasma electrolysis oxide coatings on Mg Li alloy. *Surf. Coat. Technol.* **2022**, *440*, 128445. [[CrossRef](#)]
12. Gebarowski, W.; Pietrzyk, S. Growth Characteristics of the Oxide Layer on Aluminium in the Process of Plasma Electrolytic Oxidation. *Arch. Met. Mater.* **2014**, *59*, 407–411. [[CrossRef](#)]
13. Yao, J.; Wang, S.; Zhou, Y.; Dong, H. Effects of the power supply mode and loading parameters on the characteristics of micro-arc oxidation coatings on magnesium alloy. *Metals* **2020**, *10*, 1452. [[CrossRef](#)]
14. Egorkin, V.; Gnedenkov, S.; Sinebryukhov, S.; Vyalii, I.; Gnedenkov, A.; Chizhikov, R. Increasing thickness and protective properties of PEO-coatings on aluminum alloy. *Surf. Coat. Technol.* **2018**, *334*, 29–42. [[CrossRef](#)]
15. Mohedano, M.; Mingo, B.; Mora-Sánchez, H.; Matykina, E.; Arrabal, R. Effects of pre-anodizing and phosphates on energy consumption and corrosion performance of PEO coatings on AA6082. *Surf. Coat. Technol.* **2021**, *409*, 126892. [[CrossRef](#)]
16. Mohedano, M.; Lopez, E.; Mingo, B.; Moon, S.; Matykina, E.; Arrabal, R. Energy consumption, wear and corrosion of PEO coatings on preanodized Al alloy: The influence of current and frequency. *J. Mater. Res. Technol.* **2022**, *21*, 2061–2075. [[CrossRef](#)]
17. Cheng, Y.; Cao, J.; Mao, M.; Peng, Z.; Skeldon, P.; Thompson, G. High growth rate, wear resistant coatings on an Al–Cu–Li alloy by plasma electrolytic oxidation in concentrated aluminate electrolytes. *Surf. Coat. Technol.* **2015**, *269*, 74–82. [[CrossRef](#)]
18. Wang, S.; Liu, X.; Yin, X.; Du, N. Influence of electrolyte components on the microstructure and growth mechanism of plasma electrolytic oxidation coatings on 1060 aluminum alloy. *Surf. Coat. Technol.* **2020**, *381*, 125214. [[CrossRef](#)]
19. Rahmati, M.; Raeissi, K.; Toroghinejad, M.R.; Hakimizad, A.; Santamaria, M. The multi-effects of K₂TiF₆ additive on the properties of PEO coatings on AZ31 Mg alloy. *Surf. Coat. Technol.* **2020**, *402*, 126296. [[CrossRef](#)]
20. Xiong, Y.; Hu, Q.; Hu, X.; Song, R. Microstructure and corrosion resistance of Ti₃O₅-HA bio-ceramic coating fabricated on AZ80 magnesium alloy. *Surf. Coat. Technol.* **2017**, *325*, 239–247. [[CrossRef](#)]
21. Sridhar, S.; Arunnellaiappan, T.; Rameshbabu, N.; Mika, S.; Viswanathan, A. Solar photocatalytic activity of nitrogen doped TiO₂ coating by micro-arc oxidation. *Surf. Eng.* **2016**, *33*, 779–786. [[CrossRef](#)]
22. Lin, T.-Y.; Zhang, X.-Y.; Huang, X.; Gong, X.-P.; Zhang, J.-J.; Hu, X.-J. Microstructure and properties of microarc oxidation coating formed on aluminum alloy with compound additives nano-TiO₂ and nano-ZnO. *Rare Met.* **2017**, *37*, 976–982. [[CrossRef](#)]
23. Raj, V.; Ali, M.M. Formation of ceramic alumina nanocomposite coatings on aluminium for enhanced corrosion resistance. *J. Mater. Process. Technol.* **2009**, *209*, 5341–5352. [[CrossRef](#)]
24. Habazaki, H.; Tsunekawa, S.; Tsuji, E.; Nakayama, T. Formation and characterization of wear-resistant PEO coatings formed on β-titanium alloy at different electrolyte temperatures. *Appl. Surf. Sci.* **2012**, *259*, 711–718. [[CrossRef](#)]
25. Al Bosta, M.M.S.; Ma, K.-J. Influence of electrolyte temperature on properties and infrared emissivity of MAO ceramic coating on 6061 aluminum alloy. *Infrared Phys. Technol.* **2014**, *67*, 63–72. [[CrossRef](#)]
26. Sreekanth, D.; Rameshbabu, N.; Venkateswarlu, K. Effect of various additives on morphology and corrosion behavior of ceramic coatings developed on AZ31 magnesium alloy by plasma electrolytic oxidation. *Ceram. Int.* **2012**, *38*, 4607–4615. [[CrossRef](#)]
27. Sreekanth, D.; Rameshbabu, N.; Venkateswarlu, K.; Subrahmanyam, C.; Krishna, L.R.; Rao, K.P. Effect of K₂TiF₆ and Na₂B₄O₇ as electrolyte additives on pore morphology and corrosion properties of plasma electrolytic oxidation coatings on ZM21 magnesium alloy. *Surf. Coat. Technol.* **2013**, *222*, 31–37. [[CrossRef](#)]
28. Tang, M.; Li, W.; Liu, H.; Zhu, L. Influence of K₂TiF₆ in electrolyte on characteristics of the microarc oxidation coating on aluminum alloy. *Curr. Appl. Phys.* **2012**, *12*, 1259–1265. [[CrossRef](#)]
29. Tang, M.; Feng, Z.; Li, G.; Zhang, Z.; Zhang, R. High-corrosion resistance of the microarc oxidation coatings on magnesium alloy obtained in potassium fluotitanate electrolytes. *Surf. Coat. Technol.* **2015**, *264*, 105–113. [[CrossRef](#)]
30. Fernández-López, P.; Alves, S.; López-Ortega, A.; José-Lombera, J.S.; Bayón, R. High performance tribological coatings on a secondary cast Al–Si alloy generated by Plasma Electrolytic Oxidation. *Ceram. Int.* **2021**, *47*, 31238–31250. [[CrossRef](#)]
31. Li, L.; Yang, E.; Yan, Z.; Xie, X.; Wei, W.; Li, W. Effect of pre-anodized film on micro-arc oxidation process of 6063 aluminum alloy. *Materials* **2022**, *15*, 5221. [[CrossRef](#)]

32. Zhao, Z.; Pan, Q.; Yan, J.; Ye, J.; Liu, Y. Direct current micro-arc oxidation coatings on Al-Zn-Mg-Mn-Zr extruded alloy with tunable structures and properties templated by discharge stages. *Vacuum* **2018**, *150*, 155–165. [[CrossRef](#)]
33. Arunnellaiappan, T.; Krishna, L.; Anoop, S.; Rani, R.; Rameshbabu, N. Fabrication of multifunctional black PEO coatings on AA7075 for spacecraft applications. *Surf. Coat. Technol.* **2016**, *307*, 735–746. [[CrossRef](#)]
34. Wang, Z.; Wu, L.; Cai, W.; Shan, A.; Jiang, Z. Effects of fluoride on the structure and properties of microarc oxidation coating on aluminium alloy. *J. Alloys Compd.* **2010**, *505*, 188–193. [[CrossRef](#)]
35. Hakimizad, A.; Raeissi, K.; Santamaria, M.; Asghari, M. Effects of pulse current mode on plasma electrolytic oxidation of 7075 Al in Na₂WO₄ containing solution: From unipolar to soft-sparking regime. *Electrochim. Acta* **2018**, *284*, 618–629. [[CrossRef](#)]
36. Hussein, R.O.; Nie, X.; O Northwood, D.; Yerokhin, A.; Matthews, A. Spectroscopic study of electrolytic plasma and discharging behaviour during the plasma electrolytic oxidation (PEO) process. *J. Phys. D Appl. Phys.* **2010**, *43*, 105203. [[CrossRef](#)]
37. Ling, K.; Mo, Q.; Lv, X.; Qin, G.; Yang, W.; Li, L.; Li, W. Growth characteristics and corrosion resistance of micro-arc oxidation coating on Al–Mg composite plate. *Vacuum* **2022**, *195*, 110640. [[CrossRef](#)]
38. Habazaki, H.; Fushimi, K.; Shimizu, K.; Skeldon, P.; Thompson, G. Fast migration of fluoride ions in growing anodic titanium oxide. *Electrochem. Commun.* **2007**, *9*, 1222–1227. [[CrossRef](#)]
39. Liu, T.-X.; Li, F.-B.; Li, X.-Z. Effects of peptizing conditions on nanometer properties and photocatalytic activity of TiO₂ hydrosols prepared by H₂TiO₃. *J. Hazard. Mater.* **2008**, *155*, 90–99. [[CrossRef](#)]

Disclaimer/Publisher’s Note: The statements, opinions and data contained in all publications are solely those of the individual author(s) and contributor(s) and not of MDPI and/or the editor(s). MDPI and/or the editor(s) disclaim responsibility for any injury to people or property resulting from any ideas, methods, instructions or products referred to in the content.